Open Access Full Text Article

ORIGINAL RESEARCH

Near-infrared light-mediated photodynamic/photothermal therapy nanoplatform by the assembly of Fe$_3$O$_4$ carbon dots with graphitic black phosphorus quantum dots

Ming Zhang[1,2]
Wentao Wang[3]
Yingjun Cui[2]
Ninglin Zhou[1,4]
Jian Shen[1]

[1]College of Chemistry and Materials Science, Jiangsu Collaborative Innovation Center for Biological Functional Materials, Jiangsu Engineering Research, Center for Biomedical Function Materials, Nanjing, Jiangsu, China; [2]Department of Biological Sciences, Florida International University, Miami, FL, USA; [3]Jiangsu Key Laboratory for Molecular and Medical Biotechnology, College of Life Sciences, Nanjing Normal University, Nanjing, Jiangsu, China; [4]Faculty of Materials Development, Nanjing Zhou Ninglin Advanced Materials Technology Company Limited, Nanjing, Jiangsu, China

Correspondence: Ninglin Zhou; Jian Shen
Jiangsu Collaborative Innovation Center for Biological Functional Materials, Jiangsu Engineering Research, Center for Biomedical Function Materials, 1 Wenyuan Road, Qixia, Nanjing, Jiangsu 210023, China
Tel +86 139 0158 6613;
+86 138 1388 9007
Email zhouninglin@njnu.edu.cn;
jshen@njnu.edu.cn

Background: Recently, combined photodynamic therapy (PDT) and photothermal therapy (PTT) has become a desired treatment for cancer. However, the development of economic, high-efficiency, and safe photosensitizers/photothermal agents remains a significant challenge.

Methods: A novel nanocomposite has been developed via the assembly of iron oxide carbon dot (Fe$_3$O$_4$-CDs) nanoparticles and black phosphorus quantum dots (genipin [GP]-polyglutamic acid [PGA]-Fe$_3$O$_4$-CDs@BPQDs), and this nanocomposite shows a broad light-absorption band and a photodegradable character.

Results: In vitro and in vivo assays indicated that GP-PGA-Fe$_3$O$_4$-CDs@BPQDs were highly biocompatible and exhibited excellent tumor-inhibition efficacy, due to the synergistic PTT and PDT via a near-infrared laser. Importantly, in vivo tumor magnetic resonance imaging (MRI) results illustrated that GP-PGA-Fe$_3$O$_4$-CDs@BPQDs can be specifically applied for enhanced T_2 MRI of tumors. This work presents the first combined application of a PDT and PTT effect deriving from BPQDs and MRI from Fe$_3$O$_4$-CDs, which may promote utilization of black BPQDs in biomedicine.

Conclusion: As expected, GP-PGA-Fe$_3$O$_4$-CDs@BPQDs displayed a dramatically enhanced ability to destroy tumor cells, due to the synergistic combination of PTT and PDT.

Keywords: black phosphorus quantum dots, biocompatible, photothermal, photodynamic, T_2 MRI

Introduction

With the development of nanobiotechnology, it is feasible to design multifunctional nanostructured materials that can simultaneously diagnose and treat cancers via the integration of molecular imaging and therapy technologies.[1–5] The integration of diagnosis and treatment, which can improve the survival rate and quality of life among postoperative patients, has provided an attractive avenue for detecting and treating cancer. Imaging-guided photothermal therapy (PTT), which is a novel therapeutic method of precision therapy, can be used to eliminate residual cancer cells completely with precise guidance in the future.[6,7] PTT converts absorbed light into thermal energy and generates local hyperthermia in the tumor mass to ablate cancer cells without causing damage to surrounding normal tissue.[8–10] Photodynamic therapy (PDT), a minimally invasive and high-efficiency anticancer approach, has recently received extensive research attention. PDT involves photosensitizers that absorb light and further transfer energy to oxygen in the surrounding tissue. Highly reactive oxygen species

(ROS), which work in the form of free radicals and singlet oxygen, can foster oxidation in cellular and subcellular compartments, including the plasma membrane, mitochondria, lysosomes, and the nuclear membrane, which finally leads to irreversible damage to tumor cells.[11,12] The drawbacks of poor penetration depth, excitation at short wavelengths (600–700 nm), and chemical-structure variation have prompted the search for alternative photosensitizers.[13] To overcome these drawbacks, several delivery approaches that are capable of stabilizing hydrophobic PDT drugs in aqueous solutions, including graphene, gold, silica nanoparticles, and black phosphorus (BP), have been demonstrated. The combination of PTT with PDT, termed phototherapy, can complete enhanced treatment efficacy by synergistic function. Therefore, the development of effective and safe photosensitizers/ PT agents with good biodegradability and biocompatibility is still highly probable.[14,15]

The failure caused by single treatment in cancer therapy has pushed researchers to explore the feasibility of combined treatments, such as combined PDT and PTT.[16] We chose ultrasmall BP nanosheets (referred to as BP quantum dots [BPQDs]) to serve as effective photosensitizers/PT agents in order to generate singlet oxygen ($^1O_2$).[17] Atomically thin BPQDs, new two-dimensional nanomaterials, have been focused on because of their distinct optical and electronic properties, as well as their promising applications.[18] Considering their unique and tremendously different physical properties compared to those of their bulk counterpart, BPQDs are thought to be a new high-efficiency photosensitizer for generating ROS, with great potential in cancer therapy. Their ability to photodegrade elements to biocompatible phosphorus oxides, their broad light absorption, and their excellent biocompatibility in living tissues further indicate that BP has the potential to be a therapeutic agent for cancer treatment.[19] In addition, BPQDs show broad absorption across the entire visible-light region, resulting in near-infrared (NIR) PT properties suitable for PTT.[20] Considering the unique electronic structure of BPQDs, we expect that it may be a new metal-free semiconductor to generate singlet oxygen, which can be further applied in catalysis and PDT applications. All the unique properties of BPQDs make them a promising new nanostructured system in terms of multimodal therapy for cancer.

Significant efforts to assist physicians in diagnosing and monitoring the response to therapy have been made using advances toward personalized therapeutic approaches and by increasing the precision of surgical techniques using multimodal imaging.[20] Researchers have already explored many methods for enhancing the accuracy and efficiency of selective localization during treatment, such as magnetic targeting, molecular targeting, and imaging guidance. In particular, magnetic targeting, which can be achieved using iron oxide nanoparticles in the treatment platform, not only locates the physical position of drugs but also simultaneously realizes the magnetic resonance imaging (MRI)-guided therapy effect.[19] The emergence of the MRI scanner in the manner of MRI offers doctors more precise information regarding tumor localization and boundary identification. Accompanied by advancements in high-performance imaging technology, high-performance all-in-one multimodal contrast agents are especially appealing and have recently gained the most attention, because they are needed for accurate diagnosis and therapy.[21] With advances in nanotechnology, a variety of different nanoparticulate systems, such as Gd(III)- or Mn(II)-based T_1 MR contrast agents and magnetic iron oxide (Fe_3O_4) nanoparticle-based T_2 MR contrast agents, have been developed for MRI applications. Our previous work has shown that Fe_3O_4 carbon dots (CDs) with good colloidal stability and high r_2 relaxivity can be prepared using a hydrothermal method. The as-prepared Fe_3O_4-CDs can be further functionalized with different functional groups to alleviate macrophage cellular uptake.[22]

Here, we prepared a highly dispersed suspension of ultrasmall BPQDs of ~3.6 nm (lateral) and thickness of ~1.26 nm using a simple liquid exfoliation technique. Considering that BPQDs have a unique property of absorbing NIR light with high tissue-penetration depth, we successfully designed a theranostic agent that integrated BP with iron oxide nanoparticles using ordinary electrostatic attraction and chemical cross-linking reaction. Based on the PD nature of BP nanosheets, we extended the new function of PDT and PTT for accurate selective localization using targeting and imaging guidance. Due to the PD/PT effect of BPQDs, the MR signal of Fe_3O_4, and the tumor-targeting and MRI-guiding ability of iron oxide nanoparticles, this nanoplatform exhibited a remarkably enhanced therapeutic effect and improved selectivity compared to traditional remedies. As expected, the BPQDs displayed a dramatically enhanced ability to eliminate tumor cells, benefiting from the synergistic combination of PTT and PDT.

Materials and methods
Materials
All chemicals were analytically pure reagents and used directly without further purification. BP bulk crystals were purchased from a commercial supplier (99.998%; XFNano Materials Tech, Nanjing, China) and stored in an N_2 glove box prior to use. Ferric ammonium citrate, methylene blue

(MB), 1-methyl-2-pyrrolidone, and polyglutamic acid (PGA; M_w 10,000) were obtained from Sigma-Aldrich without further purifications. PBS (pH 7.4), fetal bovine serum (FBS), MTT, trypsin–EDTA, and 4,6-diamidino-2-phenylindole were purchased from Thermo Fisher Scientific. 2,7-Dichlorofuorescein diacetate (DCFH-DA), 2,2,6,6-tetramethylpiperidine (TEMP), 2,7-dichlorofuorescein (DCF), 5-*tert*-butoxycarbonyl-5-methyl-1-pyrroline *N*-oxide (BMPO) disodium, and anthracene-9,10-dipropionic acid (Na₂-ADPA) were purchased from J&K Scientific. Other reagents were obtained from Energy Chemical (Shanghai, China). The deionized water used in all of the experiments was Milli-Q (18.2 MΩcm). All cells were purchased from the Cell Bank of Type Culture Collection of the Chinese Academy of Sciences (Shanghai, China). A genetically unrelated healthy adult donor was identified in the University of Nanjing Drum Tower Hospital Blood Donor Center donor list. The study was done after receipt of patients' written informed consent. Animal experiments were carried out in accordance with the *Guide for the Care and Use of Laboratory Animals*. All experiments were conducted in conformity with the institutional guidelines of Nanjing Normal University. Ethical approval for the in vivo animal and blood-based experiments was obtained from the National Health and Family Planning Commission. Written informed consent from the blood donors was obtained for these experiments.

Instruments and characterization

Transmission electron microscopy (TEM) and high-resolution TEM (HRTEM) images were acquired using a JEM-2100F (JEOL, Tokyo, Japan). Atomic force microscopy (AFM) was performed with a Veeco (New York, NY, USA) microscope. X-ray photoelectron spectroscopy (XPS) was conducted using a Thermo Fisher Scientific Escalab 250Xi. X-ray diffraction (XRD) patterns were obtained using a Max-3A (Rigaku, Tokyo, Japan). Ultraviolet (UV)-visible spectroscopy measurements were acquired with a Cary 5000 (Agilent Technologies, Santa Clara, CA, USA). ζ-Potential measurements and dynamic light-scattering (DLS) analysis were performed using Zetasizer Nano ZS90 (Malvern Instruments, Malvern, UK). ROS were observed using electron-spin resonance (ESR; ESP300E; Bruker, Billerica, MA, USA). To monitor temperature changes at tumor sites during irradiation, IR thermal images were observed using a PTT monitoring system (MG33; Magnity Electronics, Shanghai, China). Fluorescence and photoluminescence (PL) spectra were collected using fluorescence spectrophotometry (FluoroSens; Gilden Photonics, Glasgow, UK). Absorbance

for MTT assays was assessed with a Thermo Reader at a wavelength of 490 nm. MRI (Trio TIM 3 T; Siemens, Munich, Germany) was employed to test T_2 relaxation times. Details of the methods used for material characterization are described in the Supplementary material.

Results and discussion
Synthesis and characterization

A surface coordination strategy to enhance the stability of BPQDs in water and air by preventing the oxidation of BPQDs is described.[23] BPQDs have a well-known puckered honeycomb structure in which a phosphorus atom is covalently bonded to three neighboring single-layer phosphorus atoms, which exposes a lone pair of electrons. The lone pair of electrons in the BPQDs can readily react with oxygen to form P_xO_y. Occupation of the lone-pair electrons by other elements may prevent a reaction between phosphorus and oxygen, which ultimately mitigates the BPQDs.[24] Magnetic nanoparticles were designed to react with BPQDs to form genipin-wrapped PGA-Fe₃O₄-CDs@BPQDs, which help enhance stability in water (Figure 1A).

TEM and AFM were employed to observe the morphology of the BPQDs. The TEM images in Figure 1B (a) and Figure S1A reveal ultrasmall BPQDs of 3.6±0.6 nm. DLS measurements showed that the average diameter of the BPQDs was 6 nm (Figure S1B). This value is also consistent with the size determined from TEM, because DLS measures the overall hydrodynamic size of particles. The HRTEM image in Figure 1B (b) shows lattice fringes of 0.34 nm, which were ascribed to the (021) plane of the BPQD crystal. A typical AFM image of the BPQDs is shown in Figure S2A, and heights of the nanoparticles labeled with lines 1, 2, and 3 were 1.12, 1.27, and 1.34 nm (Figure S2B). According to statistical analysis of BPQDs under AFM, their average height was 1.26±0.8 nm (Figure S2C). BPQDs were further characterized via XPS, and showed $2p_{3/2}$ and $2p_{1/2}$ doublets at 129.4 and 129.9 eV, respectively, which are characteristic of crystalline BPQDs (Figure 2A). Furthermore, strong subbands that corresponded to oxidized phosphorus were apparent at 133.8 eV, which have been observed in a previous paper.[18] The emission wavelength of the BPQDs (Figure S3A) shifted from 380 to 500 nm when the excitation wavelength was gradually increased from 480 to 560 nm. The λ_{ex}-dependent emission of the BPQDs can be ascribed to effects from particles of different sizes in the sample and a distribution of different emission sites on each QD. λ_{ex}-dependent PL behavior is useful for multicolor in vitro and in vivo biological imaging applications.
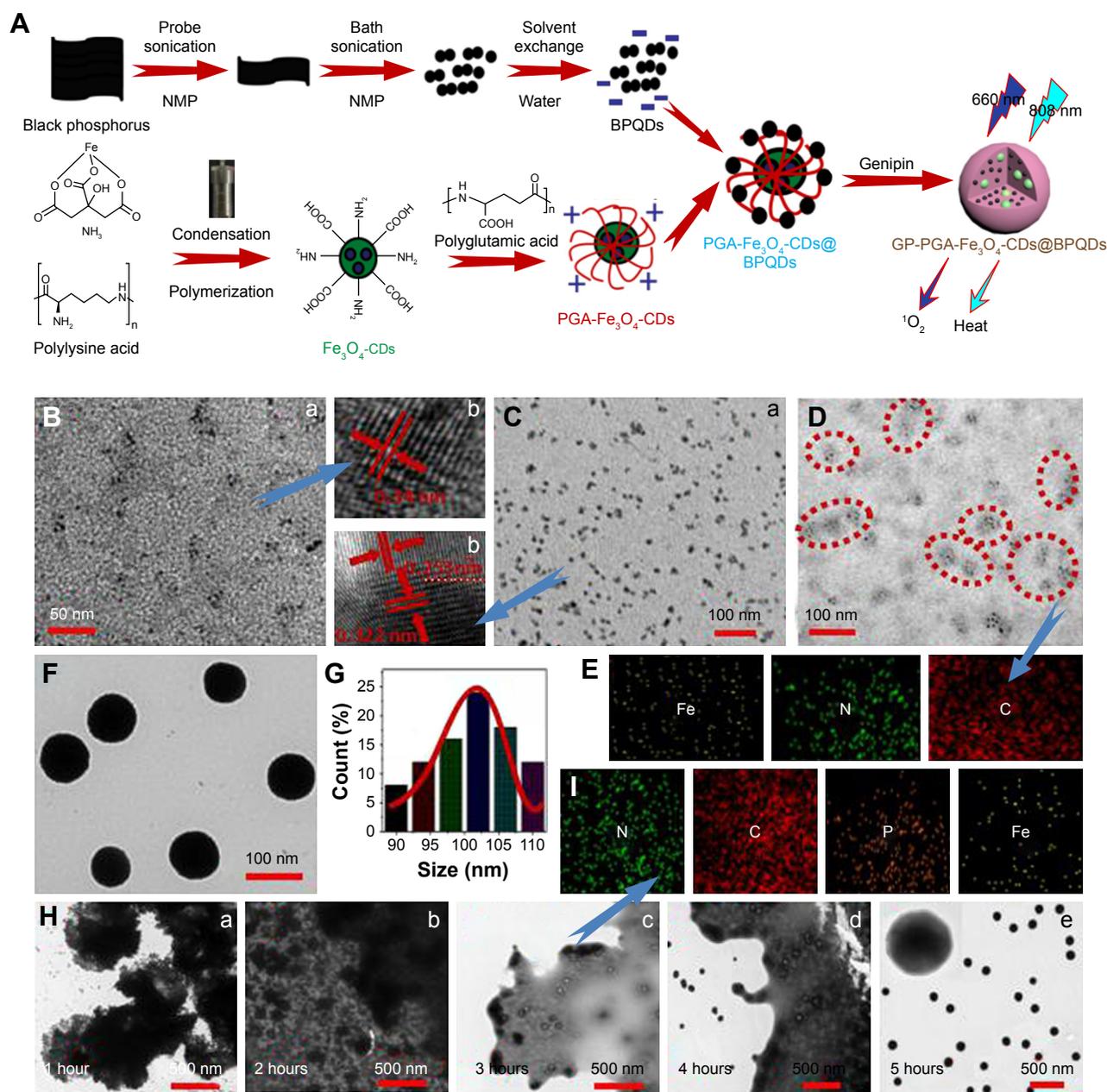
Figure 1 Preparation of GP-PGA-Fe₃O₄-CDs@BPQDs nanoplatform.
Notes: (**A**) Fabrication of the GP-PGA-Fe₃O₄-CD@BPQD nanoplatform; (**B**) TEM (a) and HRTEM (b) of BPQDs; (**C**) TEM (a) and HRTEM (b) of Fe₃O₄-CDs; (**D**) TEM of PGA-Fe₃O₄-CDs; (**E**) elemental mapping images of PGA-Fe₃O₄-CDs; (**F**) TEM of GP-PGA-Fe₃O₄-CDs@BPQDs; (**G**) lateral sizes of 50 GP-PGA-Fe₃O₄-CDs@BPQDs determined using TEM; (**H**) TEM showing the morphology of GP-PGA-Fe₃O₄-CD@BPQD assemblies and corresponding cross-linking degree of GP at different cross-linking times; (**I**) elemental mapping images of GP-PGA-Fe₃O₄-CDs@BPQDs assemblies after 3 hours of cross-linking.
Abbreviations: GP, genipin; PGA, polyglutamic acid; CD, carbon dot; BPQD, black phosphorus quantum dot; HRTEM, high-resolution transmission electron microscopy; NMP, N-methyl-2-pyrrolidone.

BPQD dispersion under 365 nm UV-light exhibited strong green emission, as shown in the inset in Figure S3A. The fluorescence quantum yield (Φ) of the as-prepared BPQDs was calculated to be 8.6%.

The morphology and structures of the resultant Fe₃O₄-CDs were further elucidated via TEM. Figure 1C (a) shows that Fe₃O₄-CDs were nearly uniform in size and shape, with an average diameter of 9.6 nm. HRTEM of an individual

Fe₃O₄-CD (Figure 1C [b]) further reveals that the nanoparticles were composed of Fe₃O₄ nanocrystals clustered in the core region and CDs assembled on their surface. Figure 1C (b) displays HRTEM of the sectional nanoparticles that show single CDs and an Fe₃O₄ nanocrystal. From the 2D lattice fringes of the CDs, an interplanar distance of ~0.322 nm was determined, which corresponded to the (006) lattice planes of graphitic (sp²) carbon. A region of magnetite (Fe₃O₄)
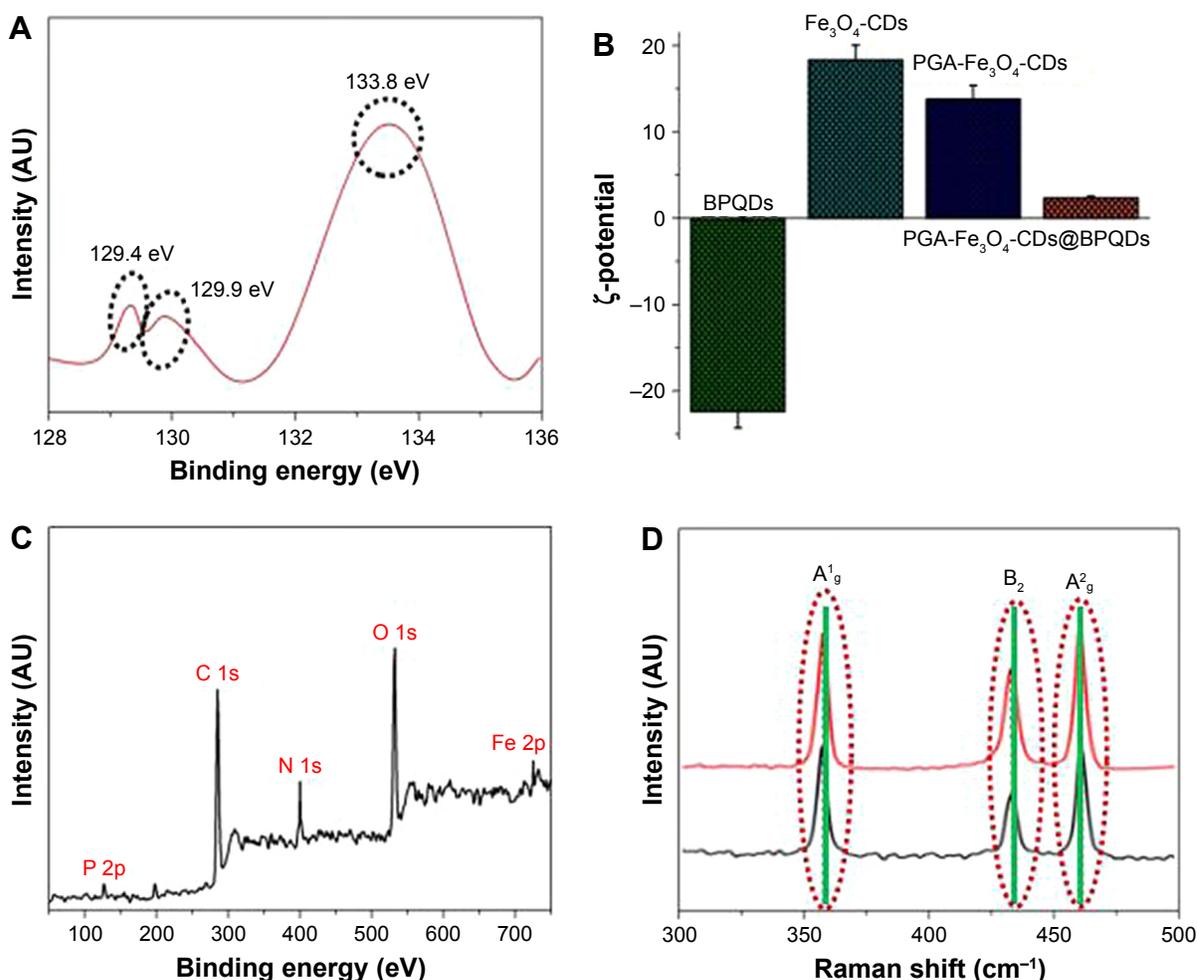
Figure 2 Characterization of GP-PGA-Fe$_3$O$_4$-CDs@BPQDs nanoplatform.
Notes: (**A**) XPS spectrum of the P 2p peaks from the BPQDs; (**B**) ζ-potential of as-prepared samples from different steps; (**C**) survey XPS spectrum of GP-PGA-Fe$_3$O$_4$-CDs@BPQDs; (**D**) Raman scattering spectra of BPQDs and GP-PGA-Fe$_3$O$_4$-CDs@BPQDs.
Abbreviations: XPS, X-ray photoelectron spectroscopy; BPQDs, black phosphorus quantum dots; GP, genipin; PGA, polyglutamic acid; CDs, carbon dots.

within the CDs can be identified by the (400) lattice spacing of 0.253 nm.[25] To obtain structural information about Fe$_3$O$_4$-CDs, XRD characterization was conducted. Six diffraction lines (Figure S3B) were observed in the representative XRD pattern of Fe$_3$O$_4$-CDs at 2θ = 30.2°, 35.5°, 43.1°, 53.5°, 57.1°, and 62.6°. These diffraction lines can be assigned as (220), (311), (400), (422), (511) and (440) reflections, respectively, of the pure cubic spinel crystal structure of Fe$_3$O$_4$, with a cell constant a=8.39 Å (Joint Committee on Powder Diffraction Standards card 19-0629).[26] Using the PGA polymer and coating strategy reported here, multifunctional magnetic fluorescent PGA-Fe$_3$O$_4$-CD hybrid nanoparticles were also obtained. Figure 1D shows TEM images of PGA polymer-coated Fe$_3$O$_4$-CDs in cluster formations. The Fe$_3$O$_4$-CD clusters consisted of an average of eight Fe$_3$O$_4$-CDs. To confirm further the formation of the hybrid nanoparticles, energy-dispersive X-ray spectroscopy

(EDS) element mapping was recorded, which is shown in Figure 1E. The EDS element mapping clearly shows that C, Fe, and N were evenly distributed in the PGA-Fe$_3$O$_4$-CD hybrid nanoparticles. It can be seen from the EDS element-mapping results that PGA had good distribution with Fe$_3$O$_4$ particles. The initial Fe$_3$O$_4$-CDs had a ζ-potential of 19.8 mV, which changed to 13.2 mV when they were modified with PGA (Figure 2B).

PGA-Fe$_3$O$_4$-CDs@BPQDs were synthesized using a simple electrostatic attraction between BPQDs and PGA-Fe$_3$O$_4$-CD nanoparticles. The ζ-potentials of the BPQDs and the PGA-Fe$_3$O$_4$-CDs were −22.7 and 13.2 mV, respectively (Figure S4A). This is the reason for the excellent electrostatic attraction reaction of PGA-Fe$_3$O$_4$-CD nanoparticles with BPQDs. Then, genipin (GP)-PGA-Fe$_3$O$_4$-CDs@BPQDs were readily synthesized via the self-polymerization of genipin according to our previous methods.[20] We determined from

typical TEM images that the resultant GP-PGA-Fe_3O_4-CDs@ BPQDs were spherical with an average diameter of 102±8 nm (Figure 1F and G) and the size of GP-PGA-Fe_3O_4-CDs@ BPQDs within the accepted range, which enabled efficient uptake by tumors based on the enhanced permeability and retention (EPR) effect. Furthermore, the as-prepared GP-PGA-Fe_3O_4-CDs@BPQDs dispersed well in NaCl, PBS, FBS, and DMEM solutions and remained stable for 1 week without any detectable agglomeration (Figure S4B).

TEM was employed to observe the microsphere morphology of the GP-PGA-Fe_3O_4-CDs@BPQDs at different stages. Figure 1H shows the TEM images of compounds with varying cross-linking times. It can be seen that a micelle-like structure formed at 1 hour (Figure 1H [a]), which suggests that the assemblies between GP-PGA-Fe_3O_4-CD@BPQD nanosheets were achieved via the reaction between PGA-Fe_3O_4-CDs@BPQDs and GP. At 2 hours (Figure 1H [b]), GP-PGA-Fe_3O_4-CD@BPQD nanosheet assemblies tended to become spherical, with a size of 200±50 nm. When cross-linking was extended to 3 hours (Figure 1H [c]), the spherical assemblies became smaller, and the swollen shell markedly decreased with an increased degree of cross-linking. The elemental mapping images (Figure 1I) show good distributions of the P, Fe, C, and N elements. After cross-linking for 4 hours (Figure 1H [d]), GP-PGA-Fe_3O_4-CD@BPQD microspheres with 3D reticular structure formed, with diameters of 100±10 nm. At cross-linking of 5 hours (Figure 1H [e] and Figure S5A), uniformly dispersed GP-PGA-Fe_3O_4-CD@ BPQD microspheres with diameters of 95–105 nm were finally fabricated with rough surfaces due to cross-linking, favorable for biological applications.[27] Correspondingly, DLS measurements revealed that GP-PGA-Fe_3O_4-CDs@ BPQDs possessed a narrow size distribution, with an average diameter of 118 nm (Figure S5B).

Detailed information about the composition of the samples was provided by XPS measurements. The XPS spectrum of the sample shows the presence of P, N, C, O, and Fe in the complex (Figure 2C). In the Fe 2p spectrum (Figure S6A), the peaks for Fe $2p_{3/2}$ and Fe $2p_{1/2}$ were observed at 710.84 and 724.48 eV, which is also indicative of the formation of an Fe_3O_4 phase in the GP-PGA-Fe_3O_4-CD@BPQD nanoparticles matrix.[26] Raman scattering was further performed to characterize the GP-PGA-Fe_3O_4-CD@BPQD nanoparticles (Figure 2D). Both samples exhibited three prominent Raman peaks at 359.8, 435.2 and 462.8 cm^{-1} that could be assigned to one out-of-plane phonon mode (A^1_g) and two in-plane modes (B_{2g} and A^2_g) of BPQDs, respectively, confirming the existence of BPQDs in the GP-PGA-Fe_3O_4-CDs@BPQDs.[10]

Since Fe_3O_4-CDs and BPQDs have different fluorescence properties when excited at different wavelengths, PL spectroscopy is a great method to characterize the cross-linking. As seen in Figure S5B, the PL of GP-PGA-Fe_3O_4-CDs@ BPQDs showed the same excitation peak display as when they were tested independently (Figure S3A for BPQDs and Figure S5B for Fe_3O_4-CDs), and this result confirmed that the nanocomposites product contained Fe_3O_4-CDs and BPQDs. The inset of Figure S5B shows the aqueous medium of GP-PGA-Fe_3O_4-CDs@BPQDs, which was collected under excitation with a 365 nm laser, and GP-PGA-Fe_3O_4-CDs@BPQDs show obvious blue, with the quantum yield of GP-PGA-Fe_3O_4-CDs@BPQDs at 440 nm calculated to be ~6.8%. We subsequently tested the impact of the GP-PGA-Fe_3O_4-CDs@BPQDs on the life of the BPQDs. Comparison of the lives of BPQDs and GP-PGA-Fe_3O_4-CDs@ BPQDs showed an inconspicuous decrease from 5.81 to 4.12 ns (Figure S5C).

Photothermal properties

Figure 3A shows the absorption of GP-PGA-Fe_3O_4-CD@ BPQD nanoparticle solutions with different concentrations in the visible NIR range. Given their efficient NIR absorption between 700 and 900 nm, GP-PGA-Fe_3O_4-CDs@ BPQDs were investigated for their potential in PT ablation therapy for cancer using an 808 nm laser.[28,29] Under continuous irradiation from a 660 nm laser (0.5 W/cm²) or 808 nm laser (2 W/cm²), the temperature elevation of the aqueous dispersion containing GP-PGA-Fe_3O_4-CDs@ BPQDs at 50 μg/mL was measured (Figure 3B). The control experiment demonstrated that the temperature of pure water (without GP-PGA-Fe_3O_4-CDs@BPQDs) and GP-PGA-Fe_3O_4-CDs@BPQDs (660 nm, 10 minutes) increased only <2.0°C and 9.4°C, respectively. However, with the addition of GP-PGA-Fe_3O_4-CDs@BPQDs (808 nm, 2 W/cm²), the temperature of the aqueous dispersions increased by 28°C after 5 minutes' irradiation. These results indicated that GP-PGA-Fe_3O_4-CDs@BPQDs rapidly and efficiently converted laser energy into heat via efficient photoabsorption at 808 nm. To study the PT effect of GP-PGA-Fe_3O_4-CDs@BPQDs further, we recorded the change in temperature of a solution (50 μg/mL, 1.0 mL) as a function of time under continuous irradiation with an 808 nm laser (2 W/cm²) until the solution reached a steady-state temperature (Figure S7A). According to Figure S7B, the PT conversion efficiency reached ~34.8%. The higher PT conversion efficiency of GP-PGA-Fe_3O_4-CDs@BPQDs makes them a prospective PT coupling agent.[30]
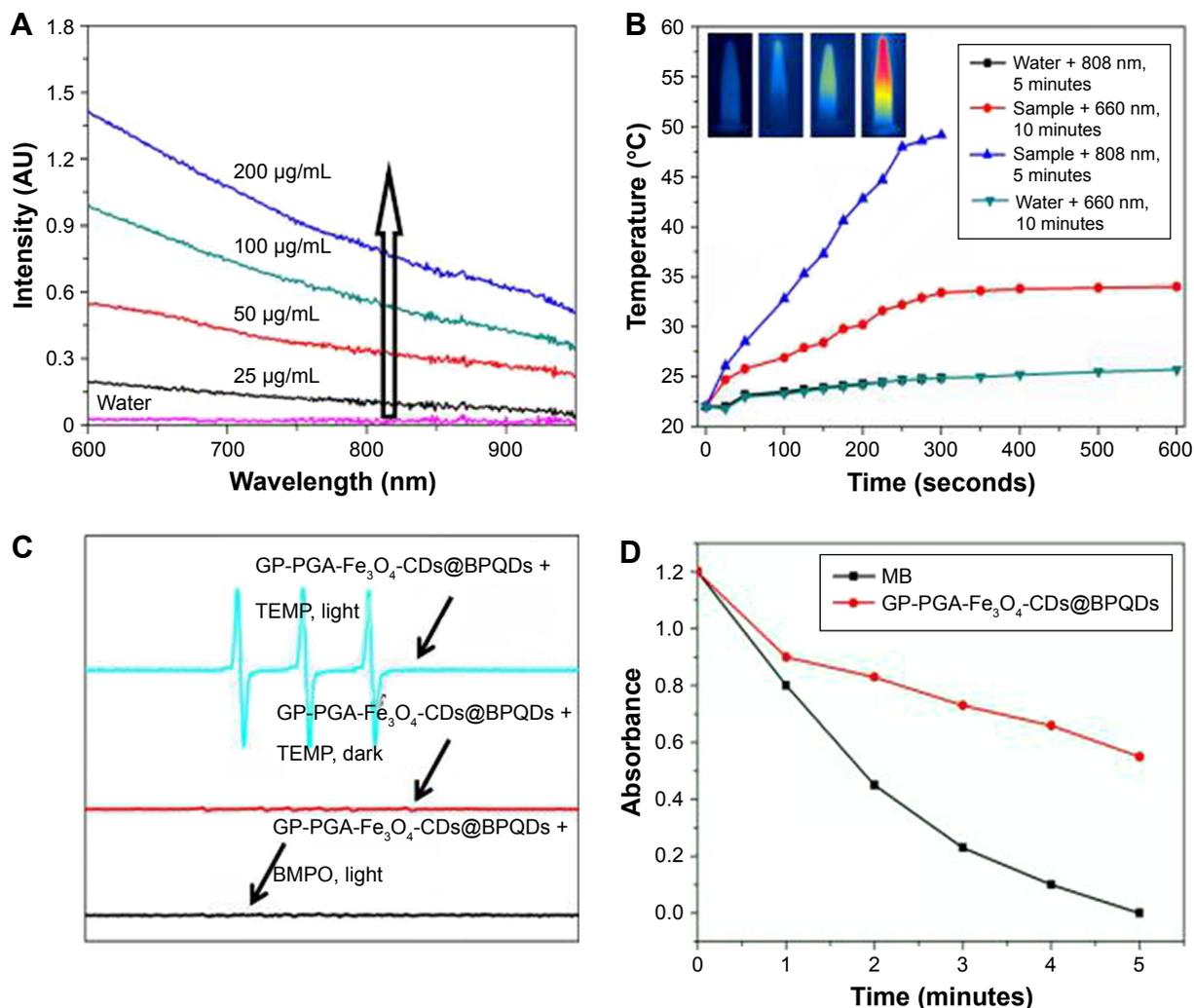
Figure 3 Photochemical and photodynamic properties of GP-PGA-Fe$_3$O$_4$-CDs@BPQDs nanoplatform.
Notes: (**A**) Ultraviolet-visible NIR-absorption spectra of GP-PGA-Fe$_3$O$_4$-CD@BPQD nanoparticle solutions at different concentrations. The arrow represents the increasing concentration of the sample. (**B**) Temperature elevation of GP-PGA-Fe$_3$O$_4$-CD@BPQD nanoparticles (50 µg/mL) under irradiation with a 660 nm (0.5 W/cm^2) or 808 nm (2 W/cm^2) laser as a function of irradiation time. Inset, temperature IR images of an aqueous solution of GP-PGA-Fe$_3$O$_4$-CDs@BPQDs under 660 nm (0.5 W/cm^2) or 808 nm (2 W/cm^2) laser irradiation, which was recorded using an IR camera. (**C**) ESR spectra of GP-PGA-Fe$_3$O$_4$-CDs@BPQDs in the presence of TEMP in different conditions. Both the decomposition of DPBF and ESR spectra were carried out under an Xe lamp with a 600 nm cutoff filter. (**D**) Decay curves of Na$_2$-ADPA absorption at 378 nm as a function of time in the presence of GP-PGA-Fe$_3$O$_4$-CDs@BPQDs and MB <660 nm laser irradiation (0.5 W/cm^2). The arrows in part C represent the curve of the sample.
Abbreviations: NIR, near-infrared; GP, genipin; PGA, polyglutamic acid; CD, carbon dot; BPQD, black phosphorus quantum dot; ESR, electron-spin resonance; TEMP, 2,2,6,6-tetramethylpiperidine; DPBF, diphenylisobenzofuran; ADPA, anthracene-9,10-dipropionic acid; MB, methylene blue; BMPO, 5-*tert*-butoxycarbonyl-5-methyl-1-pyrroline-*N*-oxide.

^{1}O$_2$ generation

ROS are generated when cells are exposed to nanomaterials. To examine the induction of oxidative stress by GP-PGA-Fe$_3$O$_4$-CDs@BPQDs, we monitored cellular ROS generation via flow cytometry using a nonfluorescent DCFH-DA that can be oxidized by intracellular ROS to become a highly fluorescent DCF. HeLa cells were treated with various concentrations of GP-PGA-Fe$_3$O$_4$-CDs@BPQDs for 3 hours under reduced serum conditions. In particular, at higher concentrations of GP-PGA-Fe$_3$O$_4$-CDs@BPQDs, ROS levels around twice as high as those of the control group were observed ([Figure S8A](#)).

ESR was used to measure the intensity of ROS generation by GP-PGA-Fe$_3$O$_4$-CDs@BPQDs under 660 nm laser irradiation. TEMP and BMPO were employed as ^{1}O$_2$ and O$_2^-$· (or OH·) trappers, respectively. Figure 3C shows a characteristic ^{1}O$_2$-induced signal only if there was TEMP-1-oxyl in the ESR spectra under laser irradiation, while Figure 3C (bottom) shows that no ROS signals were detected. These results are sufficient to verify that it was the energy rather than the electrons from GP-PGA-Fe$_3$O$_4$-CDs@BPQDs that was responsible for the transfer of oxygen during the sensitization of ground-state oxygen. Assessing the ability of GP-PGA-Fe$_3$O$_4$-CDs@BPQDs to generate ^{1}O$_2$ is thus a

definite prerequisite to avoid the inner-filter effect by which the absorption of MB and GP-PGA-Fe$_3$O$_4$-CDs@BPQDs at 660 nm were initially regulated to ~0.1 OD. ^{1}O$_2$ detection was subsequently performed via the physical method based on the direct measurement of ^{1}O$_2$ NIR luminescence at 1,270 nm. By comparing the peak areas of ^{1}O$_2$ emission at ~1,270 nm, which was induced by GP-PGA-Fe$_3$O$_4$-CDs@BPQDs and MB in a CD$_3$OD-D$_2$O mixture solution (v:v 10:1) upon 660 nm laser excitation, the ^{1}O$_2$ quantum yield of GP-PGA-Fe$_3$O$_4$-CDs@BPQDs was calculated to be 0.27 based on the given value of Φ_{MB}=0.58 in CD$_3$OD (14), as described in Figure S8B. The ^{1}O$_2$ quantum yield can also be indirectly estimated employing a chemical trapping method with Na$_2$-ADPA as the trapping agent and MB as the standard photosensitizer (Φ_{MB}=0.52 in water). As illustrated in Figure 3D, the absorbance of the Na$_2$-ADPA solution at 378 nm gradually decreased as irradiation time increased in the presence of GP-PGA-Fe$_3$O$_4$-CDs@BPQDs or MB under 660 nm laser irradiation. Based on these results, it now indicates that ^{1}O$_2$ causes the degradation of Na$_2$-ADPA when generated from GP-PGA-Fe$_3$O$_4$-CDs@BPQDs and MB. According to the decay curves of Na$_2$-ADPA absorption (Figure 3D), the ^{1}O$_2$ quantum yield of GP-PGA-Fe$_3$O$_4$-CDs@BPQDs was calculated to be 0.29. This value agrees well with ^{1}O$_2$-generation efficiency, which was estimated using the physical method.

In vivo biocompatibility

For in vivo applications, nanomaterials must have excellent blood compatibility in terms of the hemolytic effect.[31] Herein, hemolysis experiments were conducted to evaluate the blood compatibility of GP-PGA-Fe$_3$O$_4$-CDs@BPQDs. As presented in Figure 4A, the hemolytic effect of GP-PGA-Fe$_3$O$_4$-CDs@BPQDs was almost invisible by direct observation over a broad concentration range of 6.25–100 µg/mL. Hemolysis percentages increased slightly as GP-PGA-Fe$_3$O$_4$-CD@BPQD concentration increased. The hemolysis percentage of GP-PGA-Fe$_3$O$_4$-CDs@BPQDs was calculated to be 0.1%, even at a concentration of 100 µg/mL, which is lower than previously reported results of BPs@Au@Fe$_3$O$_4$ hybrids.[19] Therefore, GP-PGA-Fe$_3$O$_4$-CDs@BPQDs had negligible hemolytic activity, which is a vital characteristic for intravenous administration.

Polymers can be applied in vivo to ensure that samples mix fully with erythrocytes. Aggregation, crenation, and hemolysis are indicators of the interaction and incompatibility of samples with red blood cells (RBCs). In general, untreated RBCs in PBS have a normal biconcave shape (Figure 4B [b]).

As we know, the appearance of morphological aberrant forms of RBCs will be induced due to exposure to materials with poor blood compatibility. Figure 4B shows images of RBCs that were incubated with GP-PGA-Fe$_3$O$_4$-CDs@BPQDs. From Figure 4B (g), we can conclude that RBCs do not show any morphological changes, even at high-concentration (100 µg/mL) of GP-PGA-Fe$_3$O$_4$-CDs@BPQDs. This result agrees with the hemolysis analysis.

In vitro fluorescence imaging

The application of GP-PGA-Fe$_3$O$_4$-CDs@BPQDs to label living cells in vitro was demonstrated using HepG2 cells (human liver carcinoma cells) on confocal laser-scanning microscopy. After incubation with GP-PGA-Fe$_3$O$_4$-CDs@BPQDs (10 µg/mL) at 37°C for 6 and 12 hours, cell-emission signals were collected using continuous-wave excitation at 488 and 543 nm. As shown in Figures 4C and S9C, cell and overlay images indicate that the luminescence came from the intracellular region of HepG2 cells. The enhanced fluorescence intensity over time shows that the cellular internalization of GP-PGA-Fe$_3$O$_4$-CDs@BPQDs was time-dependent. Z-scan measurements for HepG2 cells further indicated that GP-PGA-Fe$_3$O$_4$-CDs@BPQDs had successfully entered cells. A quantitative analysis was performed to assess PL signals in living cells that were labeled with GP-PGA-Fe$_3$O$_4$-CDs@BPQDs. Figures 4C and S9C show the PL-intensity distribution for imaging in the HepG2 cells, which corresponds to a dark-field image of HepG2 cells (Figure S9A and B). As such, the 3D images confirm that GP-PGA-Fe$_3$O$_4$-CDs@BPQDs probes were internalized by the cells, rather than being bound or adsorbed on the surface of the HepG2 cells. These results suggest that GP-PGA-Fe$_3$O$_4$-CDs@BPQDs can serve as a photosensitizer/PT agent by localizing deeply into tumor cells.[32]

To ensure that efficient nucleus-targeting PDT/PTT is efficient, cancer cells have a very high intracellular uptake of nanomaterials. Therefore, we first evaluated the cellular uptake of GP-PGA-Fe$_3$O$_4$-CDs@BPQDs in HeLa cells by measuring their characteristic red fluorescence of the cells using confocal laser-scanning microscopy. The confocal images in Figures 4D and S10A clearly show that most of the red fluorescence emitted from GP-PGA-Fe$_3$O$_4$-CDs@BPQDs was distributed evenly in the cytoplasm region and the nucleus. It was clearly evident that the GP-PGA-Fe$_3$O$_4$-CD@BPQD-internalized HeLa cells exhibited a significantly higher percentage of internuclear uptake.

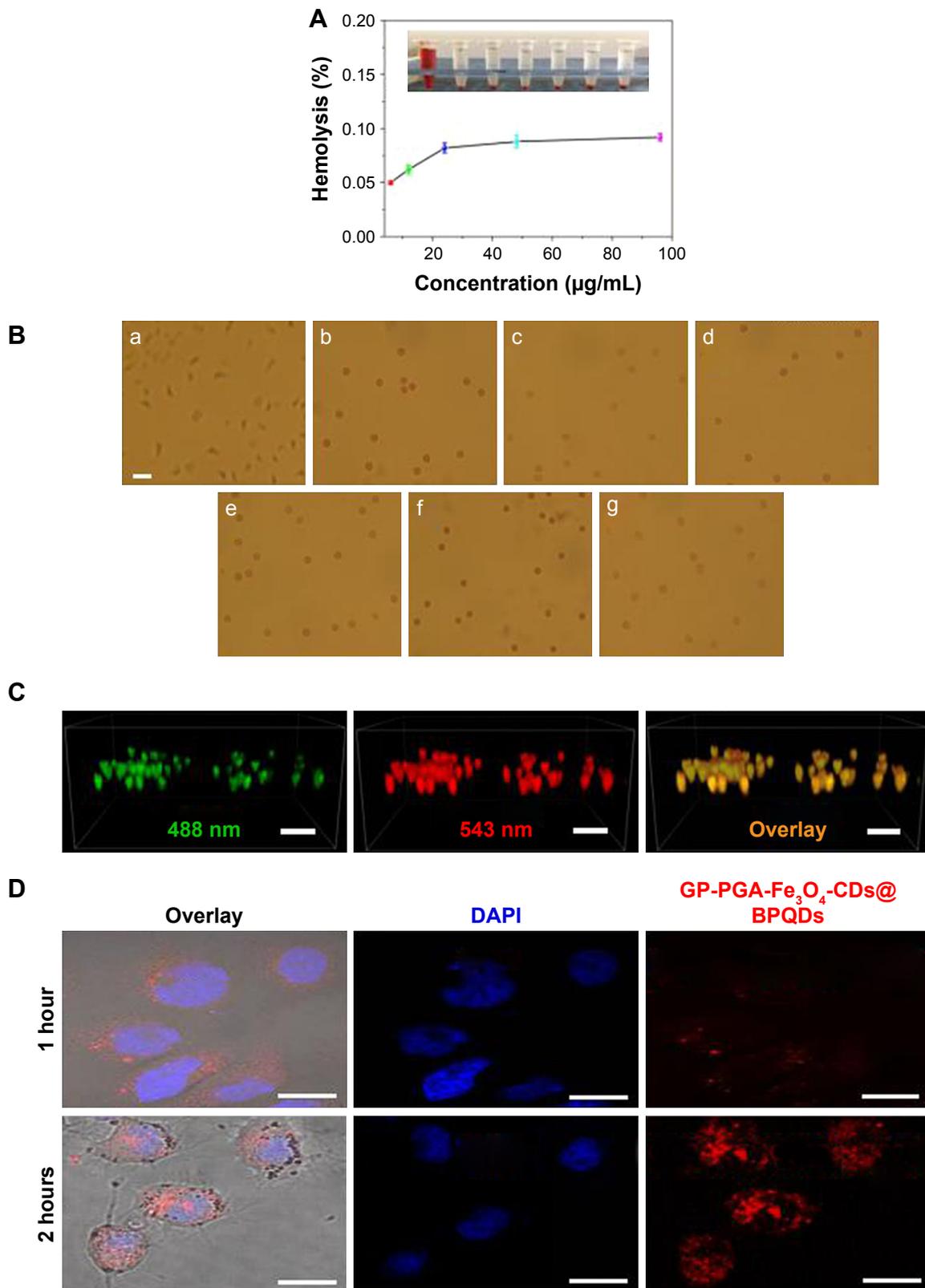Nanomaterials that are used in biomedicine must have sufficient biocompatibility. Therefore, it is necessary to

Figure 4 Blood biocompatibility and cell imaging of GP-PGA-Fe$_3$O$_4$-CDs@BPQDs nanoplatform.

Notes: (**A**) Hemolysis percentages of RBCs by GP-PGA-Fe$_3$O$_4$-CDs@BPQDs at different concentrations (upper right). Inset, supernatant from the GP-PGA-Fe$_3$O$_4$-CD@BPQD suspensions. (**B**) Optical images of RBCs treated with GP-PGA-Fe$_3$O$_4$-CDs@BPQDs: a, positive control (deionized water); b, negative control (PBS); c–f, 6.25–100 μg/mL. Scale bar =25 μm. (**C**) 3D reconstruction of the colocalization of GP-PGA-Fe$_3$O$_4$-CDs@BPQDs inside HepG2 cells after 12 hours. Scale bar =50 μm. (**D**) Confocal fluorescence images for photoexcitation of internalized red-emitting GP-PGA-Fe$_3$O$_4$-CDs@BPQDs in HeLa cells. Scale bar =25 μm.

Abbreviations: RBCs, red blood cells; GP, genipin; PGA, polyglutamic acid; CDs, carbon dots; BPQDs, black phosphorus quantum dots; DAPI, 4,6-diamidino-2-phenylindole.
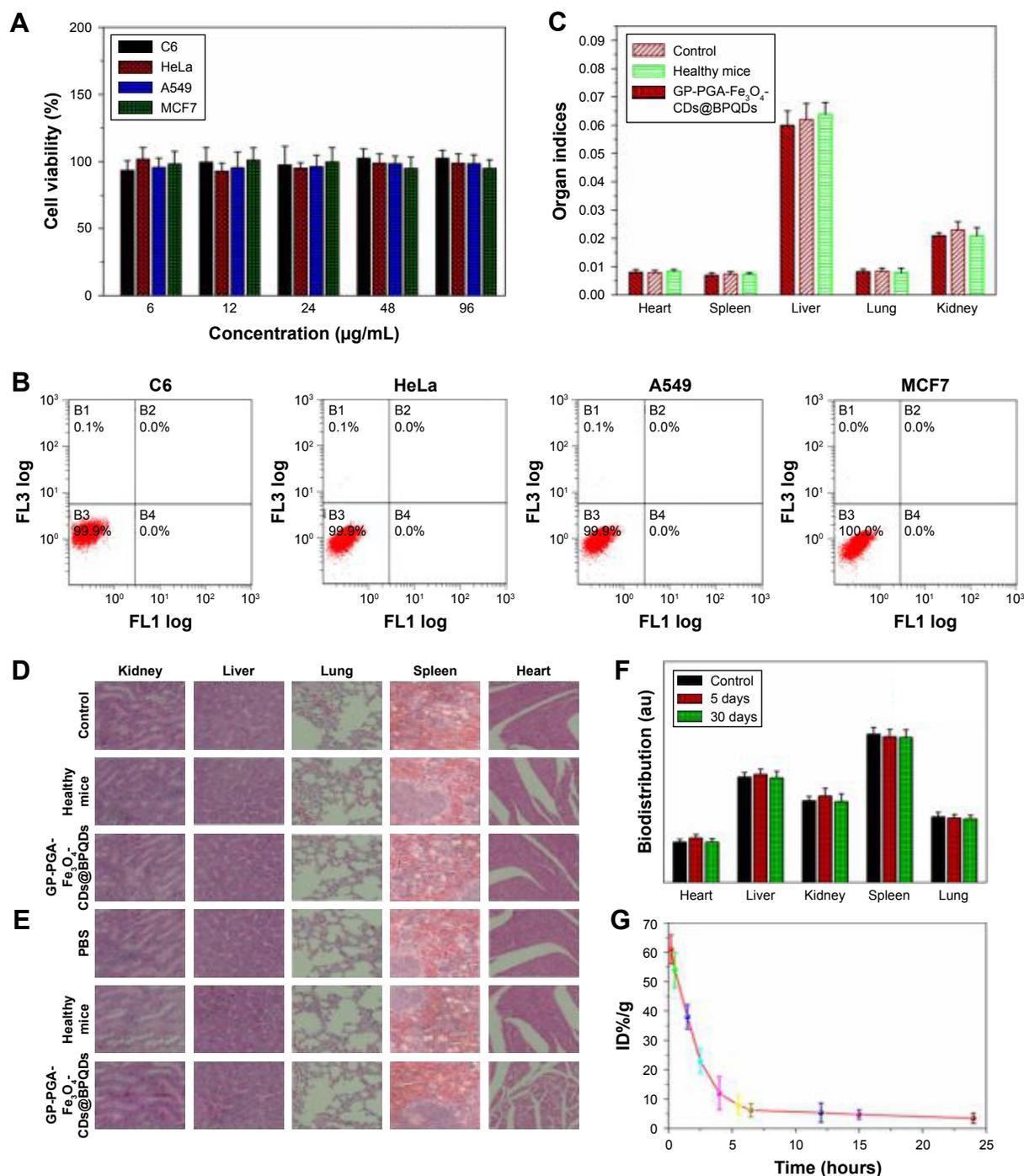
Figure 5 In vitro and vivo toxicity of GP-PGA-Fe$_3$O$_4$-CDs@BPQDs nanoplatform.
Notes: (**A**) Relative viability of C6, HeLa, A549, and MCF7 cells treated with GP-PGA-Fe$_3$O$_4$-CD@BPQD nanomicelles. (**B**) Flow-cytometry analysis of C6, HeLa, A549, and MCF7 cells before and after incubation with GP-PGA-Fe$_3$O$_4$-CDs@BPQDs. (**C**) Comparison of organ indices of mice treated with PBS, healthy, and GP-PGA-Fe$_3$O$_4$-CD@BPQD groups after 30 days. H&E-stained images of major organs from PBS, healthy mice, and mice treated with GP-PGA-Fe$_3$O$_4$-CDs@BPQDs, taken 5 days (**D**) and 30 days (**E**). (**F**) Biodistribution of P in the major organs of mice with without or GP-PGA-Fe$_3$O$_4$-CD@BPQD injection at different postinjection time points. (**G**) Blood-circulation data of GP-PGA-Fe$_3$O$_4$-CDs@BPQDs after intravenous injection.
Abbreviations: GP, genipin; PGA, polyglutamic acid; CD, carbon dot; BPQD, black phosphorus quantum dot.

ensure their low cytotoxicity to different types of cell lines (Figure 5A). A standard MTT assay was carried out to determine the relative viability of HeLa (cervical cancer), A549 (lung cancer), C6 (glioma), and MCF7 (breast cancer) cells after incubation with GP-PGA-Fe$_3$O$_4$-CDs@BPQDs at

different concentrations (6, 12, 24, 48, and 96 µg/mL) for 48 hours. No apoptosis was observed in the four cell types, even at a high concentration of 96 µg/mL (Figure 5B), which is much higher than what was used in the following PT experiments, suggesting good biocompatibility and suitability

for biomedical applications. Further, the cytocompatibility of GP-PGA-Fe$_3$O$_4$-CDs@BPQDs is determined via flow-cytometry analysis. The results in Figure 5C illustrate that the rate of cell apoptosis and necrosis did not significantly increase after the incubation of C6, HeLa, A549, or MCF7 cells with differently sized GP-PGA-Fe$_3$O$_4$-CDs@BPQDs (50 μg/mL) for 24 hours. It is proven that GP-PGA-Fe$_3$O$_4$-CDs@BPQDs have good compatibility.

In vitro cytotoxicity and in vivo ROS assay

Before moving to study in vivo antitumor combination therapy using GP-PGA-Fe$_3$O$_4$-CDs@BPQDs, we first studied the in vivo behaviors of this agent in animals using the intrinsic physical properties of GP-PGA-Fe$_3$O$_4$-CDs@BPQDs.[33] Blood was extracted from C57BL/6 mice that had been intravenously injected GP-PGA-Fe$_3$O$_4$-CDs@BPQDs at different time points postinjection. Concentrations of GP-PGA-Fe$_3$O$_4$-CDs@BPQDs in the blood were measured by the Raman signals of BPQDs.[34] As shown in Figure 5G, blood levels of GP-PGA-Fe$_3$O$_4$-CDs@BPQDs decreased gradually over time. BPQD signals in the blood remained at a reasonably high level at even 24 hours postinjection. In addition, standard biochemistry examination was performed on mice treated with GP-PGA-Fe$_3$O$_4$-CDs@BPQDs at 5 and 30 days, as shown in Figure 6A. Biochemical indices containing serum creatinine (Cr), alanine aminotransferase (ALT), total bilirubin, and aspartate aminotransferase (AST) were investigated. Here, ALT, AST, and Cr were focused on, because they have a close correlation with liver and kidney function in mice. None of AST, ALT, and Cr showed significant differences between untreated and treated mice. Furthermore, the resulting data shown in Figure 6A revealed that total bilirubin was at similar levels in mice exposed to GP-PGA-Fe$_3$O$_4$-CDs@BPQDs and control mice. Meanwhile, the results of H&E staining showed that GP-PGA-Fe$_3$O$_4$-CDs@BPQDs did not cause long-term inflammatory responses or liver and kidney toxicity (Figure 5D and E). For biodistribution analysis, the concentrations of P in major organs of mice with BPQD injection were measured by inductively coupled plasma mass spectrometry after 5 and 30 days (Figure 5F).

To confirm the exact role of $^1O_2$, ROS levels were monitored with and without preprocessing of the $^1O_2$ quencher sodium azide (NaN$_3$). From Figure 6B, it is easy to determine that ROS levels were higher in GP-PGA-Fe$_3$O$_4$-CD@BPQD-internalized HeLa cells exposed to 660 nm (0.5 W/cm^2) light than in those in the dark. Furthermore, the preprocessing of HeLa cells with NaN$_3$ significantly suppressed ROS levels in the case of 660 nm (0.5 W/cm^2) light irradiation. It is now clear from these results that under 660 nm (0.5 W/cm^2) light

photoirradiation, GP-PGA-Fe$_3$O$_4$-CDs@BPQDs induced much higher ROS levels, which resulted in significant cell death. Given their high degree of chemical reactivity, ROS disrupt organelles, such as mitochondrial membranes, upon entry into cells. Therefore, upon NIR-laser irradiation, it is anticipated that GP-PGA-Fe$_3$O$_4$-CDs@BPQDs will be able to damage tumor tissue irreversibly. DNA damage was evaluated by comet assays on HeLa cells treated with or without GP-PGA-Fe$_3$O$_4$-CDs@BPQDs (50 μg/mL), and the corresponding quantitative investigations of tail DNA and tail moment are given in Figures 6C and S10B. No obvious tail DNA or tail moment was found in the control group, while significant damage was detected in the treated group, hinting at easily identifiable DNA damage after treatment with GP-PGA-Fe$_3$O$_4$-CDs@BPQDs.[35] As a result, free-radical damage can induce cell apoptosis and further inhibit cell proliferation.

In vivo PDT/PTT

The prepared GP-PGA-Fe$_3$O$_4$-CDs@BPQDs feature green fluorescence, efficient red-light-induced generation of $^1O_2$, and heat. These features suggest that GP-PGA-Fe$_3$O$_4$-CDs@BPQDs can be used as a single cancer theranostic for PTT or PDT.[14] Staining the cells with a live/dead cell-staining kit further confirmed the excellent PT-therapy efficacy. In the laser-only (0.5 W/cm^2, 10 minutes or 2 W/cm^2, 5 minutes) treatment, green fluorescence among all cells indicated an entire survival rate (Figure 6D [a and b]). This phenomenon illustrates that heat produced from free water under laser irradiation makes no contribution to cancer-cell death. However, parts of cells are destroyed (Figure 6D [c]). They were incubated with 50 μg/mL GP-PGA-Fe$_3$O$_4$-CDs@BPQDs and laser-irradiated at 660 nm (0.5 W/cm^2, 10 minutes), due to the ease with which $^1O_2$ is generated and the inability to produce heat under 0.5 W/cm^2. Upon 660 nm laser irradiation (0.5 W/cm^2, 10 minutes), a large proportion of cells were destroyed (Figure 6D [d]). In aggregate, these results provided a function of PTT efficiency of the GP-PGA-Fe$_3$O$_4$-CDs@BPQDs and provide a plausible explanation for propelling cancer-cell death. In contrast, upon 660 nm (0.5 W/cm^2, 10 minutes) and 808 nm (2 W/cm^2, 5 minutes) laser irradiation, essentially no cells survived, as indicated by the intense homogeneous red fluorescence obtained (Figure 6D [e]). Herein, we report that GP-PGA-Fe$_3$O$_4$-CDs@BPQDs can simultaneously generate $^1O_2$ and heat to kill HeLa cells efficiently by synergistic PDT and PTT at high-power doses. The PTT/PDT effect of GP-PGA-Fe$_3$O$_4$-CDs@BPQDs was observed in both the HeLa and C6 cells (Figure S11).
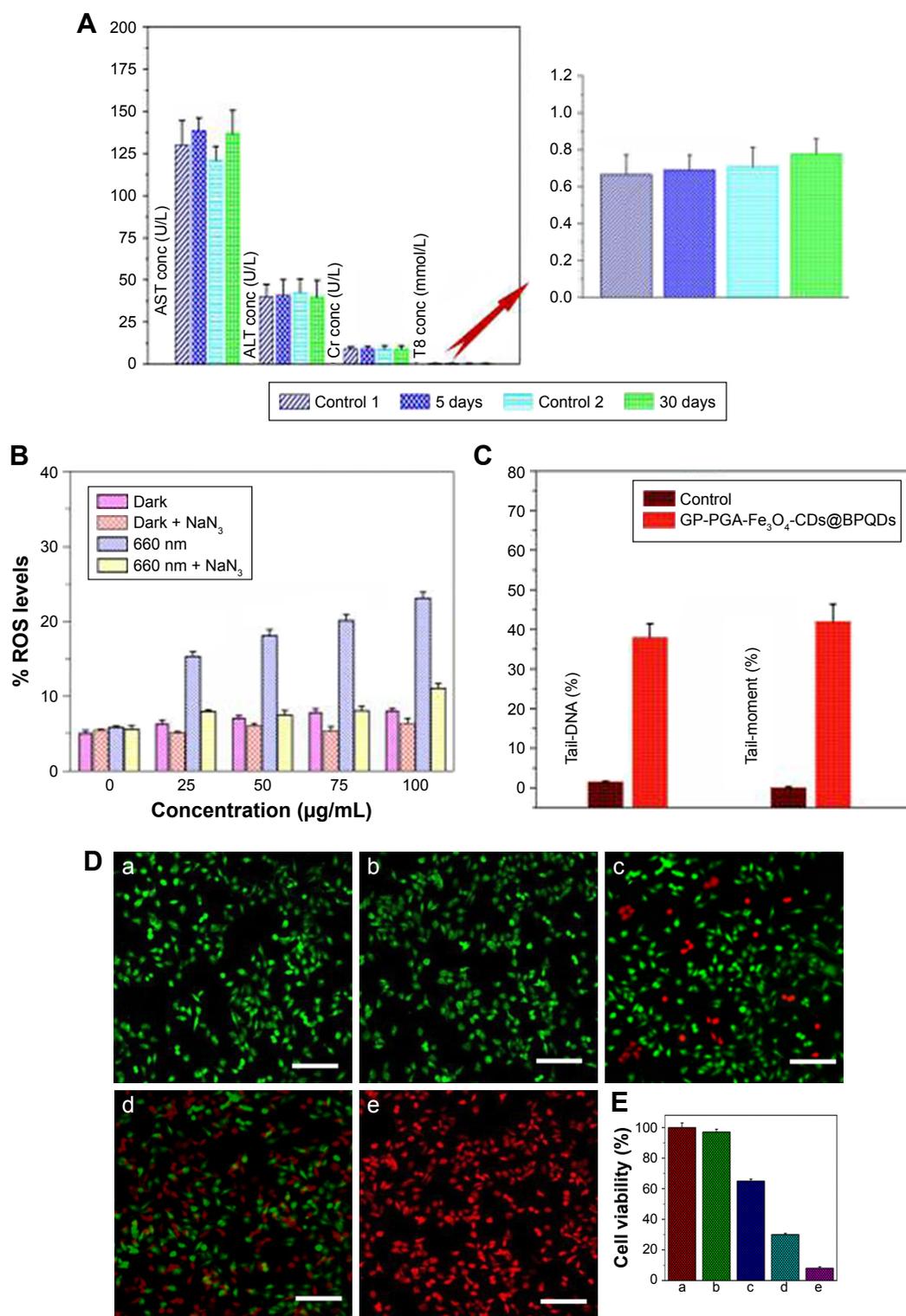
Figure 6 Cell toxicity, and ablation in vitro following incubation with GP-PGA-Fe$_3$O$_4$-CDs@BPQDs.

Notes: (**A**) Serum biochemistry data for C57BL/6 mice injected with PBS (5 and 30 days postinjection) and GP-PGA-Fe$_3$O$_4$-CDs@BPQDs (5 and 30 days postinjection). (**B**) ROS generation detected by mean fluorescence for GP-PGA-Fe$_3$O$_4$-CD@BPQD-internalized HeLa cells followed by irradiation with and without NaN$_3$ preprocessing. (**C**) Tail-DNA and tail-moment analysis. (**D**) Fluorescence images of calcein AM/PI-stained HeLa cells under various conditions: laser only (a, 0.5 W/cm^2), laser only (b, 2 W/cm^2), 50 μg/mL GP-PGA-Fe$_3$O$_4$-CDs@BPQDs + laser (c, 660 nm, 0.5 W/cm^2, PDT), 50 μg/mL GP-PGA-Fe$_3$O$_4$-CDs@BPQDs + laser (d, 808 nm, 2 W/cm^2, PTT), and 50 μg/mL GP-PGA-Fe$_3$O$_4$-CDs@BPQDs + laser (e, 660 + 808 nm, PDT/PTT). Scale bar =100 μm. (**E**) Relative viability of HeLa cells under various conditions: laser only (a, 0.5 W/cm^2), laser only (b, 2 W/cm^2), 50 μg/mL GP-PGA-Fe$_3$O$_4$-CDs@BPQDs + laser (c, 660 nm, 0.5 W/cm^2, PDT), 50 μg/mL GP-PGA-Fe$_3$O$_4$-CDs@BPQDs + laser (d, 808 nm, 2 W/cm^2, PTT), and 50 μg/mL GP-PGA-Fe$_3$O$_4$-CDs@BPQDs + laser (e, 660 + 808 nm, PDT/PTT).

Abbreviations: GP, genipin; PGA, polyglutamic acid; CDs, carbon dots; BPQDs, black phosphorus quantum dots; ROS, reactive oxygen species; AM, acetoxymethyl; PI, propidium iodide; PDT, photodynamic therapy; PTT, photothermal therapy; Cr, creatinine; ALT, alanine aminotransferase; TB, total bilirubin; AST, aspartate aminotransferase; con, concentration.

The further quantitatively studied cytotoxicity and bimodal PDT/PTT efficacy took place on GP-PGA-Fe$_3$O$_4$-CDs@BPQDs using an MTT assay. As presented in Figure 6E, a red laser by itself did not have any effect on cell survival without GP-PGA-Fe$_3$O$_4$-CDs@BPQDs. In contrast, in the PDT group (0.5 W/cm^2), cell viability decreased: 58% of cells remained alive at a high concentration of GP-PGA-Fe$_3$O$_4$-CDs@BPQDs (50 µg/mL). In the PTT groups (2 W/cm^2), cell viability drastically decreased. However, in the PDT/PTT group, a death rate ~96% was acquired, which manifests that the synergistic effects of PTT and PDT can efficiently kill HeLa cells. This result agrees with findings using calcein acetoxymethyl and propidium iodide staining.

In vivo imaging and biodistribution

Magnetic properties of the GP-PGA-Fe$_3$O$_4$-CDs@BPQDs were evaluated using a vibrating specimen magnetometer. Figure 7A shows that GP-PGA-Fe$_3$O$_4$-CDs@BPQDs
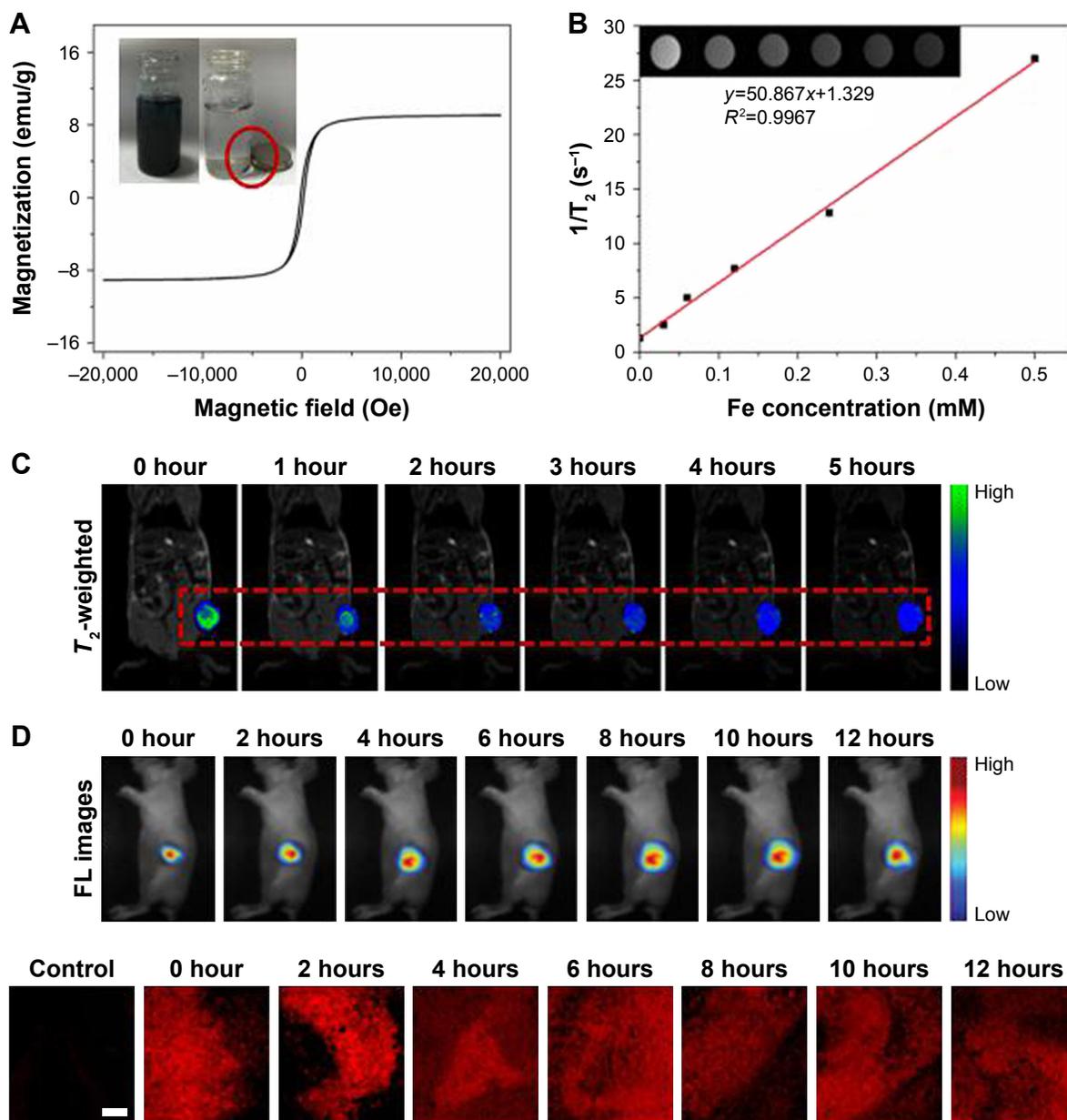

Figure 7 The distribution and biodistribution of GP-PGA-Fe$_3$O$_4$-CDs@BPQDs after injection.
Notes: (**A**) Field-dependent magnetization loop of GP-PGA-Fe$_3$O$_4$-CD@BPQD nanoparticles. Inset photos show the separation process under the magnetic field. The red circle indicates the adsorbed GP-Fe$_3$O$_4$-CDs@BPQDs. (**B**) Linear fitting of $1/T_2$ of GP-PGA-Fe$_3$O$_4$-CDs@BPQDs with different Fe concentrations. Inset: T_2-weighted MRI. (**C**) In vivo T_2-weighted MRI and color-mapped images of mice bearing tumors after intravenous injection of GP-PGA-Fe$_3$O$_4$-CDs@BPQDs at different time intervals. (**D**) Real-time in vivo fluorescence images at different injection time. (**D**) Confocal microscopy of tumor sections after subcutaneous injection of GP-PGA-Fe$_3$O$_4$-CDs@BPQDs. Scale bar =100 nm.
Abbreviations: GP, genipin; PGA, polyglutamic acid; CD, carbon dot; BPQD, black phosphorus quantum dot; MRI, magnetic resonance imaging.

exhibited ferromagnetic behavior with a hysteresis loop at 300 K, which manifested in saturation magnetization of GP-PGA-Fe$_3$O$_4$-CDs@BPQDs of 10.2 emu/g. The inset in Figure 6A shows that GP-PGA-Fe$_3$O$_4$-CDs@BPQDs were separated easily from the dispersion in water with the help of an external magnet, which suggests underlying applications of GP-PGA-Fe$_3$O$_4$-CDs@BPQDs in magnetic guidance. Based on the superparamagnetic nature and good water-dispersible property of GP-PGA-Fe$_3$O$_4$-CD@BPQD nanoparticles, the T_2-weighted MRI conducted on a 3.0 T MR scanner revealed a clear concentration-dependent darkening effect and showed a high transverse relaxivity (r_2) of 50.867×10^{-3} m/s (Figure 7B).

Tumor sizes according to T_2 modal MRI were also recorded at various time intervals in two stages: before injection and at 1, 2, 3, 4, and 5 hours after injection, as shown in Figure 7C. The contrast was more apparent (darker in the T_2-weighted MRI) in the mouse body postinjection compared to preinjection. Here, we also confirm that as synthesized, the nanoparticles simultaneously enhanced T_2 relaxation in the circulating system.[36] The enhanced signal of blood vessels was maintained for more than 5 hours, much longer than that of the Fe$_3$O$_4$ complex with a high excretion rate. These results show that GP-PGA-Fe$_3$O$_4$-CDs@BPQDs can also be used as a long-term blood-pool T_2 modal MRI contrast agent, which is very important in clinical MRI. The long-term effect is also critical for obtaining HR and steady-state images. After 5 hours, the T_2 contrast intensity in the mouse body had clearly increased, while the contrast intensity in the region of liver, kidney, and spleen had increased. In general, once injected intravenously, contrast agents easily accumulated in liver, kidney, and spleen tissue (Figure 7C). Positive-contrast enhancement of nanoparticles was achieved anatomically via transverse MRI in vivo. Precontrast and postcontrast color-mapped images of tumors in the experimental mice were recorded at the beginning.[22] T_2-weighted MRI intensity gradually declined as the time after injection of the GP-PGA-Fe$_3$O$_4$-CDs@BPQDs increased. The red box in Figure 7C shows images of the T_2 distribution of a tumor, in which the region of the tumor becomes blue with time. These results indicate that GP-PGA-Fe$_3$O$_4$-CDs@BPQDs have specificity for T_2-enhanced MRI in tumor sites.

In a separate attempt to demonstrate the potential use of GP-PGA-Fe$_3$O$_4$-CDs@BPQDs for in vivo theranostic, nude mice with HeLa tumors were used to investigate the feasibility of using nanoparticles for fluorescence imaging-guided phototherapy. When the tumors reached 80 mm^3, mice were treated with a subcutaneous injection of Cy5.5-labeled

GP-PGA-Fe$_3$O$_4$-CDs@BPQDs. The ability of Cy5.5-labeled GP-PGA-Fe$_3$O$_4$-CDs@BPQDs dispersed in PBS for in vivo fluorescence imaging was tested by injecting 20 µL Cy5.5-labeled GP-PGA-Fe$_3$O$_4$-CDs@BPQDs into mouse tumors. Fluorescence images of the mice were then detected using a Maestro 2 multispectral imager. As shown in Figure 7D, the tumor area showed a strong fluorescence semaphore. The area of the fluorescence semaphore gradually diffused from the center, which implies that GP-PGA-Fe$_3$O$_4$-CDs@BPQDs had good distribution in the tumor. This result revealed that GP-PGA-Fe$_3$O$_4$-CDs@BPQDs accumulated in the tumor site through the EPR effect, and fluorescence was able to be detected in the tumor site. Major organs and tumors were excised from the mice for biodistribution analysis. Concentrations of P in major organs of mice with GP-PGA-Fe$_3$O$_4$-CDs@BPQDs injections were measured via inductively coupled plasma mass spectrometry after 1 and 24 hours (Figure S12A). At 24 hours postinjection, large GP-PGA-Fe$_3$O$_4$-CD@BPQD concentrations were found the tumors and organs, including the lung, heart, spleen, kidneys, and liver, which was consistent with the in vivo fluorescence examination. Furthermore, confocal microscopy images of tumor sections showed that after injection, GP-PGA-Fe$_3$O$_4$-CDs@BPQDs accumulated in the tumor site via the EPR effect, and obvious fluorescence was seen in the tumor site in comparison with the control group (Figure 7D). Therefore, considerable uptake of GP-PGA-Fe$_3$O$_4$-CDs@BPQDs by tumors can be achieved due to the EPR effect.[37]

In vivo PDT/PTT

Inspired by the exciting in vitro results in our triple-mode combination therapy in vitro, we further carried out combination therapy in vivo using GP-PGA-Fe$_3$O$_4$-CDs@BPQDs in mice with HeLa tumors. The mice were classified into groups: saline as the control group, free GP-PGA-Fe$_3$O$_4$-CDs@BPQDs, GP-PGA-Fe$_3$O$_4$-CDs@BPQDs with 660 nm laser irradiation (PDT), GP-PGA-Fe$_3$O$_4$-CDs@BPQDs with 808 nm laser irradiation (PTT), and GP-PGA-Fe$_3$O$_4$-CDs@BPQDs with both 660 and 808 nm laser irradiation (PDT/PTT). To demonstrate the PT activity of GP-PGA-Fe$_3$O$_4$-CDs@BPQDs inside tumors, tumor temperature under irradiation was monitored using a thermal camera (Figure 8A and B). For the GP-PGA-Fe$_3$O$_4$-CD@BPQD-treated group (808 nm, 2 W/cm^2), tumor temperature increased to ~50°C after being irradiated for 5 minutes. For the GP-PGA-Fe$_3$O$_4$-CD@BPQD-treated group (660 nm, 0.5 W/cm^2), tumor temperature increased to ~42°C after being irradiated for 10 minutes (Figure S12B). However,
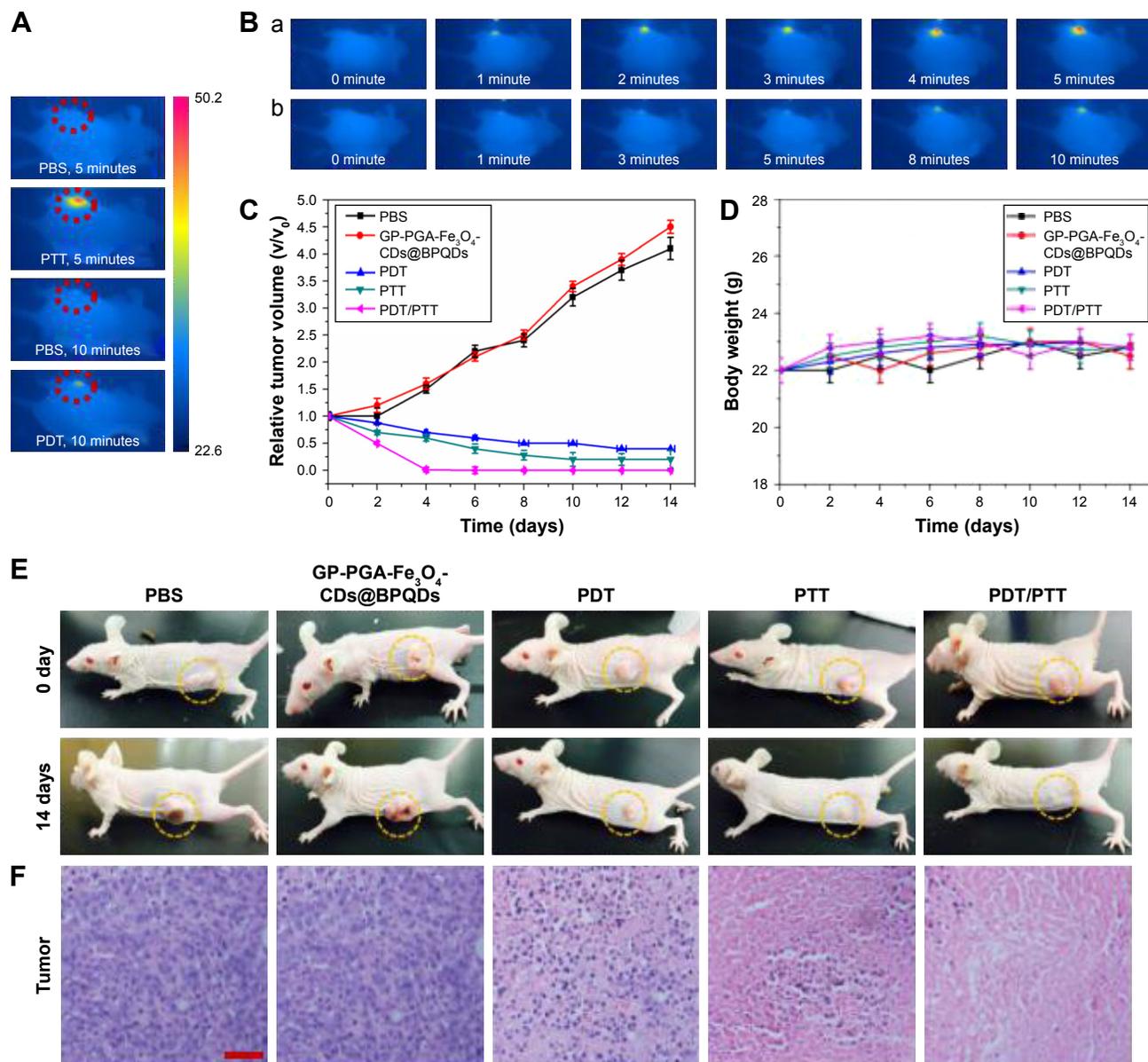
Figure 8 Therapeutic effects of GP-PGA-Fe$_3$O$_4$-CDs@BPQDs in mice exposed to NIR after injection.
Notes: (**A**) Highest temperature within the tumor area recorded by an IR camera after 660 or 808 nm laser irradiation. (**B**) Thermography of tumor-bearing mice receiving photothermal treatment for different periods: a, 808 nm, 2.0 W/cm^2, 5 min; b, 660 nm, 0.5 W/cm^2, 10 min. (**C**) Weight-growth curves. Mice were measured every 2 days. (**D**) Tumor growth curves (n=5). Measurements taken after different treatments. (**E**) Mice with HeLa tumors after various treatments. (**F**) H&E staining of tumor sections collected from different treatment groups. Scale bar =50 µm.
Abbreviations: GP, genipin; PGA, polyglutamic acid; CDs, carbon dots; BPQDs, black phosphorus quantum dots; NIR, near-infrared; PTT, photothermal therapy; PDT, photodynamic therapy.

the highest temperature of the tumor area in the PBS group was only ~35°C after being irradiated for 10 minutes, which demonstrates that the GP-PGA-Fe$_3$O$_4$-CDs@BPQDs in the treated group (808 nm, 2 W/cm^2) played a key role in heat generation.

We further investigated the in vivo therapeutic effect of GP-PGA-Fe$_3$O$_4$-CDs@BPQDs. After different treatments, tumor volumes were measured using a caliper for 14 days and normalized against their initial sizes. The free

GP-PGA-Fe$_3$O$_4$-CDs@BPQDs exhibited a therapeutic effect on the tumors (Figure 8C and E). While PDT using GP-PGA-Fe$_3$O$_4$-CDs@BPQDs with 660 nm irradiation showed a moderated growth-inhibition effect with tumor-growth inhibition (TGI) of 79.3%, PTT using GP-PGA-Fe$_3$O$_4$-CDs@BPQDs with 808 nm irradiation exhibited an improved TGI of 86.2%. Importantly, mice with the combined therapy of GP-PGA-Fe$_3$O$_4$-CDs@BPQDs plus 660 and 808 nm laser irradiation (TGI 98.8%) showed a remarkably enhanced therapeutic

effect compared with single therapy. Excised tumors from representative mice ([Figure S13](#)) show that tumors treated with GP-PGA-Fe$_3$O$_4$-CDs@BPQDs under 660 and 808 nm laser irradiation were smaller than those of other groups. In addition, tumors were excised for H&E staining after 14 days' treatment (Figure 8F). No change was detected in the PBS or free GP-PGA-Fe$_3$O$_4$-CD@BPQD groups. In the PDT and PTT groups, some inflammatory cell infiltration, cell death, and even cirrhosis with tissue-structure damage were observed. However, in the PDT/PTT group, almost all tumor-tissue cells were destroyed and became necrotic.

The weights of all mice of mice were relative (Figure 8D). The liver, heart, spleen, kidneys, and lung were collected from the mice 2 days posttreatment ([Figure S14](#)). No pathological changes were observed in the spleen, kidneys, lung, or heart for mice in the PDT/PTT group compared with those in the control group. The results suggest that GP-PGA-Fe$_3$O$_4$-CDs@BPQDs are likely good theranostic carriers for cancer treatment.[38,39] Taken together, the in vivo PDT/PTT results indicated that the GP-PGA-Fe$_3$O$_4$-CDs@BPQDs induced apparent tumor inhibition, but there was no obvious damage to the major organs in the tumor-bearing mice, which reveals a potential platform for the treatment of malignant cancers.

Conclusion

In summary, multifunctional GP-PGA-Fe$_3$O$_4$-CDs@BPQDs, as a therapeutic agent based on a new photosensitizer/PT agent (BPQDs) combined with a targeted Fe$_3$O$_4$-CD agent, were successfully fabricated for the first time using a simple, mild, and reliable approach. The developed GP-PGA-Fe$_3$O$_4$-CDs@BPQDs possess characteristics of active fluorescence, efficient $^1O_2$ generation (Φ=0.29) under 660 nm laser irradiation and high PT conversion efficiency (η=36.2%) under 808 nm laser irradiation, and prominent T_2-weighted MRI. To understand the in vivo behavior of as-obtained GP-PGA-Fe$_3$O$_4$-CDs@BPQDs regarding their biodistribution and biocompatibility, deeper exploration is required. The tumor-bearing mice recovered completely after phototherapy using nanoparticles as $^1O_2$ and heat mediators. Hematological, biochemical, and pathological analyses demonstrated that GP-PGA-Fe$_3$O$_4$-CDs@BPQDs did not give rise to long-term inflammatory reactions or obvious damage in mice. Therefore, our research emphasizes the significant potential of GP-PGA-Fe$_3$O$_4$-CDs@BPQDs in nanobiomedicine.

Acknowledgments

Disclosure

The authors report no conflicts of interest in this work.

References

1. Tan L, Wu T, Tang ZW, et al. Water-soluble photoluminescent fullerene capped mesoporous silica for pH-responsive drug delivery and bioimaging. *Nanotechnology*. 2016;27:315104.
2. Zhang M, Chi C, Yuan P, Su Y, Shao M, Zhou N. A hydrothermal route to multicolor luminescent carbon dots from adenosine disodium triphosphate for bioimaging. *Mater Sci Eng C Mater Biol Appl*. 2017;76: 1146–1153.
3. Zhang M, Yuan P, Zhou NL, Su YT, Shao MN, Chi C. pH-sensitive N-doped carbon dots: heparin and doxorubicin drug delivery system – preparation and anticancer research. *RSC Adv*. 2017;7:9347–9356.
4. Ge J, Jia Q, Liu W, et al. Red-emissive carbon dots for fluorescent, photoacoustic, and thermal theranostics in living mice. *Adv Mater*. 2015;27:4169–4177.
5. Sun Z, Xie H, Tang S, et al. Ultrasmall black phosphorus quantum dots: synthesis and use as photothermal agents. *Angew Chem Int Ed Engl*. 2015;127:11688–11692.
6. Noh MS, Lee S, Kang H, et al. Target-specific near-IR induced drug release and photothermal therapy with accumulated Au/Ag hollow nanoshells on pulmonary cancer cell membranes. *Biomaterials*. 2015; 45:81–92.
7. Zhang M, Wang WT, Yuan P, Chi C, Zhang J, Zhou NL. Synthesis of lanthanum doped carbon dots for detection of mercury ion, multi-color imaging of cells and tissue, and bacteriostasis. *Chem Eng J*. 2017;330: 1137–1147.
8. Zhang M, Zhou NL, Yuan P, Su YT, Shao MN, Chi C. Graphene oxide and adenosine triphosphate as a source for functionalized carbon dots with applications in pH-triggered drug delivery and cell imaging. *RSC Adv*. 2017;7:9284–9293.
9. Sun C, Wen L, Zeng J, et al. One-pot solventless preparation of PEGylated black phosphorus nanoparticles for photoacoustic imaging and photothermal therapy of cancer. *Biomaterials*. 2016;91:81–89.
10. Shao J, Xie H, Huang H, et al. Biodegradable black phosphorus-based nanospheres for in vivo photothermal cancer therapy. *Nat Commun*. 2016;7:12967.
11. Vankayala R, Kuo CL, Nuthalapati K, Chiang CS, Hwang KC. Nucleus-targeting gold nanoclusters for simultaneous in vivo fluorescence imaging, gene delivery, and NIR-light activated photodynamic therapy. *Adv Funct Mater*. 2015;25:5934–5945.
12. Su YT, Zhang M, Zhou NL, et al. Preparation of fluorescent N, P-doped carbon dots derived from adenosine 5′-monophosphate for use in multicolor bioimaging of adenocarcinomic human alveolar basal epithelial cells. *Microchim Acta*. 2017;184:699–706.
13. Li WW, Rong PF, Yang K, Huang P, Sun K, Chen XY. Semimetal nanomaterials of antimony as highly efficient agent for photoacoustic imaging and photothermal therapy. *Biomaterials*. 2015;45:18–26.
14. Ge J, Jia Q, Liu W, et al. Carbon Dots with Intrinsic Theranostic Properties for Bioimaging, Red-Light-Triggered Photodynamic/Photothermal Simultaneous Therapy In Vitro and In Vivo. *Adv Healthc Mater*. 2016; 5(6):665–675.
15. Gollavelli G, Ling YC. Magnetic and fluorescent graphene for dual modal imaging and single light induced photothermal and photodynamic therapy of cancer cells. *Biomaterials*. 2014;35:4499–4507.

16. Chen WS, Ouyang J, Liu H, et al. Black phosphorus nanosheet-based drug delivery system for synergistic photodynamic/photothermal/chemotherapy of cancer. *Adv Mater*. 2017;29:1603864.

17. Sun ZB, Zhao YT, Li ZB, et al. TiL$_4$-coordinated black phosphorus quantum dots as an efficient contrast agent for in vivo photoacoustic imaging of cancer. *Small*. 2017;13:1602896.

18. Wang H, Yang XZ, Shao W, et al. Ultrathin black phosphorus nanosheets for efficient singlet oxygen generation. *J Am Chem Soc*. 2015;137:11376–11382.

19. Yang D, Yang GX, Yang PP, et al. Assembly of Au plasmonic photothermal agent and iron oxide nanoparticles on ultrathin black phosphorus for targeted photothermal and photodynamic cancer therapy. *Adv Funct Mater*. 2017;27:1700371.

20. Zhang M, Wang WT, Cui YJ, Zhou NL, Shen J. Magnetofluorescent carbon quantum dot decorated multiwalled carbon nanotubes for dual-modal targeted imaging in chemo-photothermal synergistic therapy. *ACS Biomater Sci Eng*. 2018;4:151–162.

21. Yuan Y, Ding ZL, Qian JC, et al. Casp3/7-instructed intracellular aggregation of Fe$_3$O$_4$ nanoparticles enhances T$_2$ MR imaging of tumor apoptosis. *Nano Lett*. 2016;16:2686–2691.

22. Zhang M, Wang WT, Wu F, Yuan P, Chi C, Zhou NL. Magnetic and fluorescent carbon nanotubes for dual modal imaging and photothermal and chemo-therapy of cancer cells in living mice. *Carbon*. 2017;123:70–83.

23. Zhao YT, Wang HY, Huang H, et al. Surface coordination of black phosphorus for robust air and water stability. *Angew Chem Int Ed Engl*. 2016;128:5087–5091.

24. Li LK, Yu YJ, Ye GJ, et al. Black phosphorus field-effect transistors. *Nat Nanotechnol*. 2014;9:372–377.

25. Justin R, Tao K, Román S, et al. Photoluminescent and superparamagnetic reduced graphene oxide-iron oxide quantum dots for dual-modality imaging, drug delivery and photothermal therapy. *Carbon*. 2016;97:54–70.

26. Fan YT, Sun QY, Gu H, et al. GO-COO-HP-β-CD nanosphere: a complex construction and its drug-loading properties. *Nanotechnology*. 2014;25:255601.

27. Sun HM, Cao LY, Lu LH. Magnetite/reduced graphene oxide nanocomposites: one step solvothermal synthesis and use as a novel platform for removal of dye pollutants. *Nano Res*. 2011;4:550–562.

28. Zhang M, Wang J, Wang WT, Zhang J, Zhou NL. Magnetofluorescent photothermal micelles packaged with GdN@CQDs as photothermal and chemical dual-modal therapeutic agents. *Chem Eng J*. 2017;330:442–452.

29. Zhou J, Lu ZG, Zhu XJ, et al. NIR photothermal therapy using poly-aniline nanoparticles. *Biomaterials*. 2013;34:9584–9592.

30. Chen Q, Liu XD, Zeng JF, Cheng ZP, Liu Z. Albumin-NIR dye self-assembled nanoparticles for photoacoustic pH imaging and pH-responsive photothermal therapy effective for large tumors. *Biomaterials*. 2016;98:23–30.

31. Yuan P, Zhang M, Zhou NL, et al. N-doped CDs-GP nanospheres as a drug delivery nanocarrier system with carbon dots and a fluorescent tracer. *New J Chem*. 2017;41:10880–10889.

32. Xia A, Chen M, Gao Y, Wu DM, Wei F, Li FY. Gd^{3+} complex-modified NaLuF$_4$-based upconversion nanophosphors for trimodality imaging of NIR-to-NIR upconversion luminescence, X-ray computed tomography and magnetic resonance. *Biomaterials*. 2012;33:5394–5405.

33. Liu JJ, Wang C, Wang XJ, et al. Mesoporous silica coated single-walled carbon nanotubes as a multifunctional light-responsive platform for cancer combination therapy. *Adv Funct Mater*. 2015;25:384–392.

34. Liu Z, Davis C, Cai WB, He L, Chen XY, Dai HJ. Circulation and long-term fate of functionalized, biocompatible single-walled carbon nanotubes in mice probed by Raman spectroscopy. *Proc Natl Acad Sci U S A*. 2008;105:1410–1415.

35. Zhang M, Wang WT, Zhou NL, et al. Near-infrared light triggered photo-therapy, in combination with chemotherapy using magneto-fluorescent carbon quantum dots for effective cancer treating. *Carbon*. 2017;118:752–764.

36. Kobayashi H, Brechbiel MW. Nano-sized MRI contrast agents with dendrimer cores. *Adv Drug Deliv Rev*. 2005;57:2271–2286.

37. Mu XY, Wang JY, Bai XT, et al. Black phosphorus quantum dots induced oxidative stress and toxicity in living cell and mice. *ACS Appl Mater Int*. 2017;9:20399–20409.

38. Bao CC, Conde J, Pan F, et al. Gold nanoprisms as a hybrid in vivo cancer theranostic platform for in situ photoacoustic imaging, angiography, and localized hyperthermia. *Nano Res*. 2016;9:1043–1056.

39. Havrdova M, Hola K, Skopalik J, et al. Toxicity of carbon dots: effect of surface functionalization on the cell viability, reactive oxygen species generation and cell cycle. *Carbon*. 2016;99:238–248.